

X-ray studies of various shapes of electron-velocity distribution functions and of electron confinement affected by kilovolt-range electrostatic potentials

T. Cho, M. Hirata, E. Takahashi, K. Ogura,* K. Masai,† N. Yamaguchi,
T. Kondoh,‡ K. Matsuda, H. Hojo, M. Inutake, K. Ishii, Y. Kiwamoto, A. Mase,
T. Saito, K. Yatsu, and S. Miyoshi

Plasma Research Centre, University of Tsukuba, Tsukuba, Ibaraki 305, Japan

(Received 17 May 1991)

Several types of x-ray diagnostics, such as x-ray energy spectrum analyses, x-ray absorption methods, and x-ray tomographic reconstructions using various types of x-ray detectors (i.e., a Si(Li), a pure Ge, a NaI(Tl), Si surface-barrier detectors, as well as microchannel plates) have been employed for obtaining various shapes of electron-velocity distribution functions as well as their spatial profiles: (i) a plateau-shaped electron-velocity distribution function in the plug region, supporting a scaling theory between thermal-barrier potentials and ion-confining potentials (Cohen's strong electron-cyclotron heating theory); (ii) mirror-trapped 60-keV relativistic Maxwellian electrons in the thermal-barrier region; and (iii) two-component Maxwellian electrons in the central cell have been observed in the tandem-mirror GAMMA 10. During experiments with thermal barriers, it has been observed that the bulk-electron temperature and its evolution with time in the central cell are quite different from the electron energy and its temporal evolution in the plug region. These differences as well as the different shape of the electron-velocity distribution function in each region have clearly demonstrated the existence of a thermal-isolation effect due to the thermal barriers between the central cell and the plug region. X-ray tomography data in these three regions have shown good axisymmetric radial profiles peaked on the magnetic axis; this axisymmetric shape is useful for reducing nonambipolar radial particle losses. Furthermore, the validity of the Pastukhov theory for electron-energy confinement that is enhanced due to the formation of thermal-barrier potentials has been demonstrated using the electron-energy balance analyses. These data have represented a good electron-energy confinement capability due to the formation of thermal barriers.

PACS number(s): 52.55.Pi, 52.50.Gj, 52.55.Jd, 52.70.La

I. INTRODUCTION

Recent developments in rf plasma heating, particularly in electron-cyclotron heating (ECH) [1–5], have enhanced the importance of soft-x-ray diagnostics with temporal and spatial resolution.

In tandem-mirror devices [6], the second-harmonic ECH ($\omega \approx 2\Omega_e$) in the barrier region (barrier ECH) [7,8] is utilized for the formation of a thermal-barrier potential ϕ_b , which reduces the electron heat flow between the central cell and the plug region. The fundamental ECH ($\omega \approx \Omega_e$) is employed for the formation of an ion-confining potential ϕ_c in the plug region (plug ECH) [9]. The enhancement of ϕ_c is theoretically predicted with increasing ϕ_b [6,10] because of the efficient heating of localized plug electrons; these are thermally isolated from a large volume of central-cell electrons when ϕ_b is formed.

Therefore, it is important to investigate electron-velocity distribution functions using x-ray diagnostics in these thermally isolated regions (i.e., the plug, the central-cell, and the barrier regions), since these electron distribution functions are directly affected by electrostatic potentials in the kilovolt range, although these regions are connected through magnetic-field lines. These kilovolt-range potentials may form various shapes of distribution functions in the thermally separated regions. These studies on electrons affected by such electrostatic

potentials or electric fields may also give useful information on recent mechanism studies of H modes in tokamak devices [11]; the relation between the electric-field configuration and the H -mode transition has attracted wide attention.

These x-ray diagnostics are utilized for the following physical mechanism studies. (i) The scaling law between the values of ϕ_c and ϕ_b is theoretically predicted by Cohen's strong ECH theory [10]. This is one of the most important scaling laws in thermal-barrier tandem mirrors [6], since economical fusion plants are possible only when the efficient formation of ϕ_c enhanced by ϕ_b is realized. For clarifying the physical bases of the scaling law, the measurements of the electron-velocity distribution function in the plug region are essential, since the scaling law between ϕ_c and ϕ_b theoretically requires a special type of the plug electron distribution function; namely, a plateau-shaped electron-velocity distribution function. In this manuscript an observation of the plateau-shaped plug electron distribution function obtained from plug x-ray diagnostics has been described in more detail as compared with our preliminary report [12] along with the comparison with Cohen's scaling theory [10]. (ii) The x-ray observation in the barrier region shows that the barrier ECH produces hot electrons with 60-keV energy. The physical mechanism of the hot-electron production is explained in terms of second-harmonic electron-cyclotron

wave damping, corrected for the effects of the relativistic-mass variation and the Doppler shift (for more detail, see Refs. [7] and [8]). Though the plug and the barrier regions exist in the same magnetic mirror, drastic differences not only in their temperatures but also in the shapes of electron-velocity distribution functions have been obtained; the effects of electrostatic potential on these electrons are discussed as well. (iii) The x-ray data in the central cell are used for electron-energy-balance studies so as to estimate the electron-energy confinement time τ_{Ee} [13]. In this manuscript, a presentation of the scaling law of τ_{Ee} has been made; the comparison with the Pastukhov theory [14] modified by Cohen *et al.* [15] is carried out for clarifying an important effect of ϕ_b on the central-cell electron-energy confinement. (iv) In addition to the individual experimental results in the three regions, the different shapes of the electron-velocity distribution functions as well as their spatial electron profiles are then compared, and their relations are discussed.

This report describing the electron behavior through these three main regions in a tandem-mirror device along with their relations will provide essential information for the understandings of the thermal-barrier tandem-mirror physics, as well as for the bases of important scaling laws of ϕ_c vs ϕ_b and of τ_{Ee} .

II. EXPERIMENTAL APPARATUS

The experiments have been carried out in GAMMA 10, which is a minimum- B anchored tandem mirror with outboard axisymmetric plug and barrier cells (Fig. 1). It has an axial length L of 27 m, and the total volume of the improved vacuum vessel is 150 m³. The central cell has a length of 6 m and a limiter with a diameter of 36 cm, and the magnetic-field intensity at the midplane B_m is 0.405 T with a mirror ratio R_m of 5.2. Ion-cyclotron heating (6.2 MHz, 200 kW) is employed for producing hot ions in the range of kilo-electron-volts. The plug and barrier cells are axisymmetric mirrors; they have a diameter of 1.5 m and an axial length of 2.5 m ($B_m = 0.497$ T, $R_m = 6.2$, and $B_m / (\partial B_m / \partial r) = 6-10$ m). Microwaves (28 GHz, 140 kW) are injected in the extraordinary mode into the plug

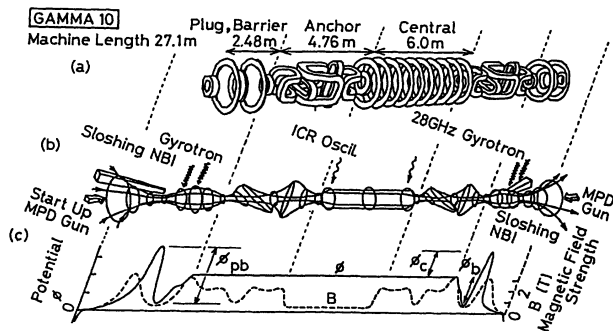


FIG. 1. Schematic view of the tandem-mirror GAMMA 10 (MPD denotes magnetoplasma dynamic; NBI means neutral-beam injection; ICR means ion-cyclotron frequency range); (a) magnetic coil set; (b) magnetic-flux tube with heating systems; (c) axial magnetic field (dashed curve) and potential profiles (solid curve).

and the barrier regions to produce ϕ_c and ϕ_b . Neutral beams (25 keV, 20 A) are injected to produce slushing ions in the plug and barrier regions. Also, recently installed helium cryogenic-panel pumping systems with a pumping speed of 2.7×10^6 l/s are employed. Thereby, a drastic reduction of wall recycling and a significant improvement of charge-exchange losses are achieved.

The x-ray diagnostic systems in each region are as follows:

(i) In the plug region, the energy spectra, from x-ray pulse-height analyses (PHA), ranging from 0.7 to 150 keV, are measured with a Si(Li) detector (depletion layer $p = 0.27$ cm, with an $8\text{-}\mu\text{m}$ Be window), and simultaneously with a pure Ge detector ($p = 1$ cm, with a 0.125-mm Be window) as shown in Fig. 2. An x-ray computer tomography technique using microchannel plates (MCP) with 50 channels is applied for a two-dimensional reconstruction of the x-ray emissivity. Here, we use the detailed calibration data on the MCP [16-19] as a function of x-ray energy from 0.06 to 82 keV and incident angle; these have been investigated using synchrotron radiation from the storage ring at the Photon Factory of the National Laboratory for High Energy Physics (KEK) for precise x-ray data analyses. To estimate electron-velocity distribution functions, the x-ray absorption method [4,7] is also employed, using polypropylene (PP), polyester (PE), and aluminum (Al) absorbers.

(ii) In the barrier region, the x-ray PHA using a NaI(Tl) detector (see Fig. 3) (5 cm thick, 2.5 cm in diameter, with a 2-mm aluminum entrance window) as well as a pure Ge detector is employed to measure the photon spectrum from 1.8 to 750 keV (with more than a 10% detection efficiency) [7,8]. Two systems of the MCP (50 channels for each system) are installed near the midplane of the plug and barrier mirror (in the thermal-barrier region) (see Fig. 4). The x rays from hot electrons (60 keV)

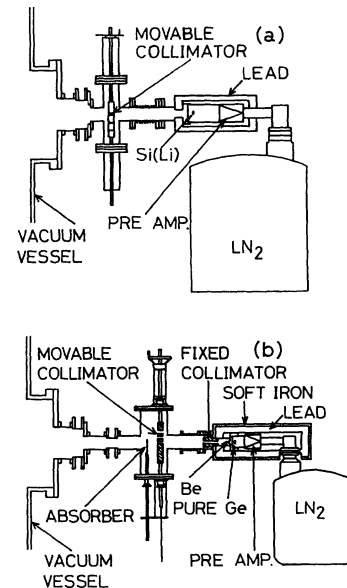


FIG. 2. Schematic view of soft-x-ray pulse-height analysis systems (LN₂ means liquid nitrogen): (a) with a Si(Li) detector and (b) with a pure Ge detector.

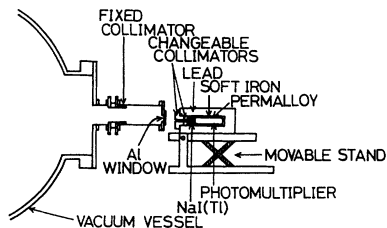


FIG. 3. Schematic view of a soft-x-ray pulse-height analysis system with a NaI(Tl) detector.

are imaged on the MCP through a pinhole (3 mm in diameter); the spatial resolution in the midplane of the plasma is 3 cm [7,20]. Here, the x-ray absorption method is also employed for analyzing the two-dimensional spatial distribution of the hot electrons.

(iii) In the central cell, the x-ray PHA with a Si(Li) detector is utilized for the observation of the temperature and the density of a warm-electron component in the energy range of a few keV; this component is produced in the plug region and then flows into the central cell through a “loss cone” in the velocity space of the plug region (see Sec. III A). X-ray tomographic reconstructions

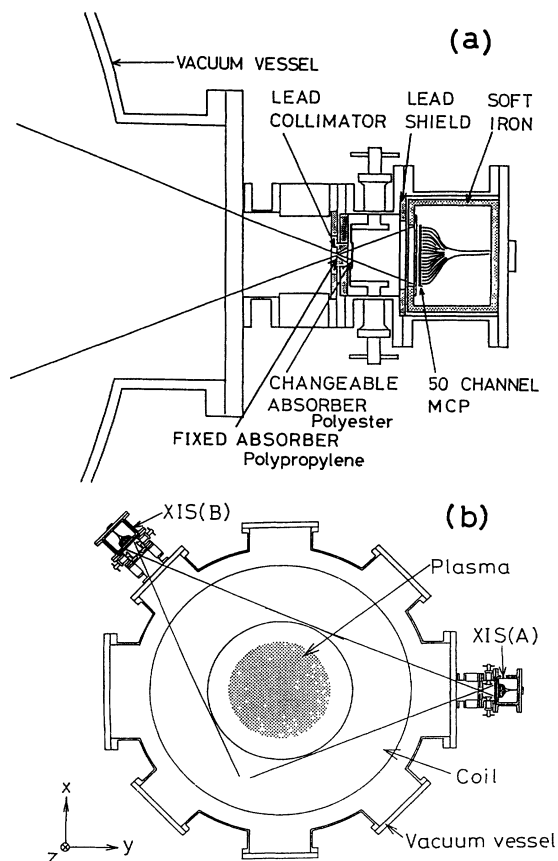


FIG. 4. Schematic view of (a) temporally and spatially resolved x-ray imaging system (XIS) with a multiple-anode microchannel plate (MCP), and (b) two sets of x-ray tomography systems (50 channels for each system).

using the MCP are suitable for the observation of the bulk-electron component with hundreds of eV energy because of its high gain even in the energy range of several tens of eV [16]. Also, silicon surface-barrier (SSB) detectors, which are precisely calibrated using synchrotron radiation [18,21], are used for the purpose of measuring the warm-electron component because of its good sensitivity to x rays in the kilo-electron-volt range [18,21]; these SSB data are useful to cross-check the data obtained with the Si(Li) and the MCP detectors. As described below, the warm-electron component is important, since this component is a main heating source for the central-cell bulk electrons through a collisional energy-relaxation process.

Potential diagnostics are as follows. The radial profile of the plug potential Φ_p is measured with multigridded electrostatic end-loss-ion energy analyzers (ELA) [9] and an E||B end-loss-ion spectrometer (ELIS) from the Upgraded Tandem Mirror Experiment (TMX-U) at Lawrence Livermore National Laboratory (LLNL) [9,22]. The central-cell potential Φ_c , and the barrier potential Φ_B at the thermal-barrier midplane are directly measured with heavy-ion (Au^0) beam probes [23]. The radial profile of Φ_B is obtained every 1 ms in one shot. Thus, we can calculate the potentials as $\phi_c = \Phi_p - \Phi_c$ and $\phi_b = \Phi_c - \Phi_B$ [9]. Also, a plug electron-confining potential ϕ_{pb} is obtained as $\Phi_p - \Phi_B$ (i.e., $\phi_c + \phi_b$).

III. EXPERIMENTAL RESULTS AND DISCUSSION

In this section a presentation of data sets for the electron-velocity distribution functions and for x-ray spatial profiles in the main regions of a tandem-mirror device (i.e., the plug region, the thermal-barrier region, and the central cell) is made along with the discussions on their relations.

A. The electron-velocity distribution function in the plug region f_{ep} and its relation to the plug electron-confining potential ϕ_{pb}

One of the most important fundamental principles for ion confinement in tandem mirrors is the formation of an electrostatic potential ϕ_c for the end-loss-ion plugging. Electron heating due to plug ECH plays an important role in the formation of ϕ_c . Therefore, for clarifying the mechanism of the formation of ϕ_c , it is essential to study the electron-velocity distribution function in the plug region f_{ep} as well as to investigate the relation between ϕ_c and f_{ep} .

As described in Sec. I, ϕ_c is expected to be enhanced by the formation of ϕ_b , because of the thermal-isolation effect of ϕ_b on the plug electrons. Thus, the study of the relation between ϕ_c and ϕ_b along with the effects of ϕ_c and ϕ_b on f_{ep} is one of the most important issues.

In Fig. 5 the data with the ratio of the plug to the central-cell densities $n_p/n_c = 0.40-0.50$ are plotted. This shows a strong correlation between the values of ϕ_c and ϕ_b . Here, we use ELA (filled circles) and ELIS (open circles) for the observation of Φ_p . These scaling data are extended as compared with those in our preliminary report [12]. On the other hand, the relation between ϕ_c

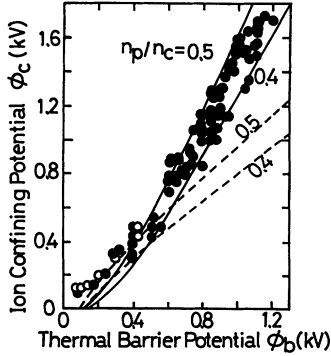


FIG. 5. Scaling data on ϕ_c vs ϕ_b ; filled circles and open circles correspond to the data measured with ELA and ELIS for the observation of the plug potential, respectively. These data with $n_p/n_c=0.40-0.50$ are compared with theoretical results predicted by Cohen's theories of strong (solid curves) and weak (dashed curves) ECH.

and ϕ_b is predicted by Cohen's weak (dashed curves) and strong (solid curves) ECH theories [10,24,25]. Figure 5 shows a transition from the weak [24] through the intermediate [25], and then to the strong ECH prediction [10] with increasing ϕ_b . It is important to note that this transition is expected to be accompanied by a change in f_{ep} from a Maxwellian to a plateau-shaped velocity distribution function, since a remarkable thermal-isolation effect due to the ϕ_b increase causes an efficient heating of plug localized electrons. Thereby, Coulomb collisions of the electrons for a Maxwellian formation are drastically reduced, and f_{ep} is then distorted from Maxwellian to a plateau shape. From this viewpoint, the observation of f_{ep} in this high- ϕ_b region is essential for clarifying the physical mechanism and for establishing the physics bases of the scaling law between ϕ_c and ϕ_b .

The strong ECH theory is constructed under the axial configuration of ϕ_b , ϕ_c , and ϕ_{pb} , as shown in Fig. 6(a). A schematic drawing of f_{ep} expected from the strong ECH theory is depicted in Fig. 6(b) [10]. This velocity space is divided into the following three regions: The ϕ_{pb} -trapped electrons are confined in the regime *P*, where the plateau

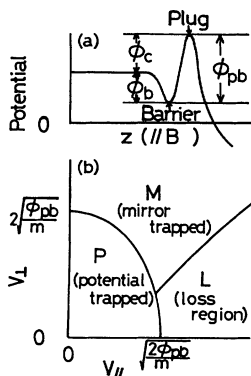


FIG. 6. Schematic drawings of (a) an axial potential profile, and (b) a model of a plug electron-velocity distribution function f_{ep} due to the strong ECH theory.

electrons formed by the acceleration of a perpendicular velocity component v_\perp due to plug ECH are bounded by an ellipsoidal separatrix [10]. The Maxwellian electrons, which are accelerated beyond the separatrix and then trapped by the plug and barrier mirror with a temperature T_{pm} , are located in the region *M* in Fig. 6(b); these electrons are heated by both plug and barrier ECH. The electrons in the region *L* are lost from the plug region through the loss cone with an angle $\theta_0=35^\circ$. A fraction of these electrons flows into the end region along the magnetic-field lines; however, they are reflected by radially and azimuthally insulated segmented floating end plates with a kilovolt-range negative potential. The other fraction of the "loss electrons" from the plug region (originally oriented to the central cell), along with the above-mentioned reflected electrons, flows in the direction of the central cell; these kilo-electron-volt range electrons (warm electrons) then become a heating source for the central-cell bulk electrons due to the Coulomb interaction process (see Sec. III D).

The x-ray PHA data in the plug region are shown as recorded with the Si(Li) detector; these data are taken during the period with plug ECH [Fig. 7(a)] as well as at 5 ms after the turn-off time of plug ECH [Fig. 7(b)]. In Fig. 7(b), ϕ_{pb} has already decayed to 0, but the other heating powers are still being injected. A comparison between Figs. 7(a) and 7(b) shows a remarkable feature of the quick decay of the x rays at $h\nu \lesssim 5$ keV in the case with $\phi_{pb}=0$ [Fig. 7(b)] as compared with $2\phi_{pb}=5.4$ kV [Fig. 7(a)]. However, a higher-energy component, continued to at least 7 keV, does not change in either case. For the observation of these higher-energy x-rays, the data with the pure Ge detector are also represented in Fig. 7(c) for $2\phi_{pb}=5.4$ kV and in Fig. 7(d) for $\phi_{pb}=0$. These spectra from the high-energy electron component observed with both detectors consistently show the same electron temperature of 60 keV.

For the x-ray spectrum analyses, the relativistic Born approximation [26–28] corrected by the Elwert factor

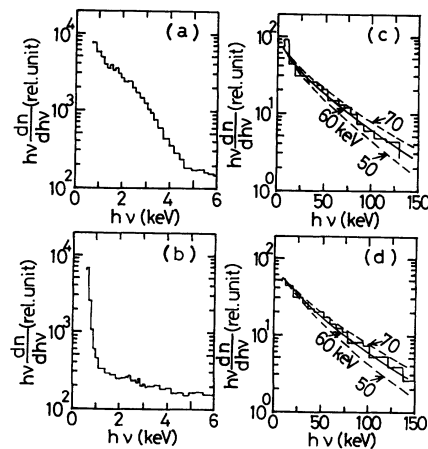


FIG. 7. X-ray energy spectra in the plug region. Data for (a) $2\phi_{pb}=5.4$ kV and (b) $\phi_{pb}=0$ using the Si(Li) detector as well as data on a high-energy component for (c) $2\phi_{pb}=5.4$ kV and (d) $\phi_{pb}=0$ using the pure Ge detector are shown.

[29] is used for the values of the x-ray cross section [7,12,26–28]. The x-rays emitted at the detector angle [27,28] are calculated using various plateau distribution functions depending on ϕ_{pb} [see Fig. 6(b)] as well as relativistic Maxwellian distributions [7] with various T_{pm} and θ_0 . Figure 8 shows examples of x-ray spectra calculated from the plateau electrons in the strong ECH theory [Fig. 6(b)] due to electron-ion interactions (the solid curve) and electron-electron interactions (the dashed curve) under the condition of $2\phi_{pb}=5.4$ kV. There is no appreciable line radiation from both *K* and *L* shells [30–32] as seen in Fig. 7; hence, impurities in the plasmas are ignored for the analyses (for more details see Ref. [20]).

X-ray observations with a NaI(Tl) detector in the barrier region also show the same electron temperature of 60 keV as measured in the plug region (see Sec. III B). These 60-keV electrons observed in both the barrier and the plug regions support the existence of the plug and barrier mirror-trapped electrons as predicted in the region *M* [Fig. 6(b)] from Cohen's strong ECH theory [10]. Even after the ϕ_{pb} decay, such mirror-trapped high-energy electrons continue to be confined in the plug and barrier mirror because of their low collisionality (see again Figs. 7(b) and 7(d) as well as Ref. [7]). Therefore, this electron component is not directly related to ϕ_{pb} .

On the other hand, intense x-rays from the lower-energy electron component below 5 keV are observed only when ϕ_{pb} is formed [Fig. 7(a)]. This means that the electrons emitting this x-ray component are closely related to ϕ_{pb} . To identify their velocity distribution functions, the spectrum in Fig. 7(a) is fitted using the calculated results from relativistic Maxwellian distributions; however, the dotted curves labeled with 2 and 1 keV in Fig. 9(a) can fit the data ranging up to 2.5 keV alone, and

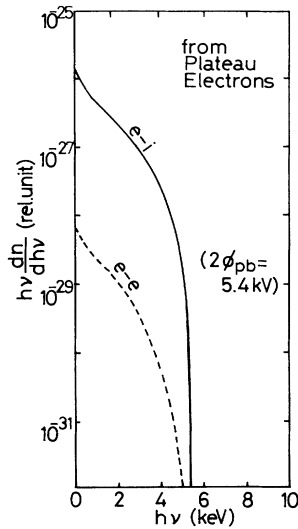


FIG. 8. Calculated x-ray spectra emitted from the plateau electrons within the ellipsoidal boundary with $2\phi_{pb}=5.4$ kV [see the region *P* in Fig. 6(b)]. The solid curve is calculated due to the electron-ion interactions and the dashed curve is due to the electron-electron interactions. Here, the relativistic Born approximation corrected by the Elwert factor is used.

exceeding 2.5 keV alone, respectively. No Maxwellian combinations can fit the spectrum with $\kappa=d\ln(h\nu dn)/d(h\nu)^2 < 0$, since the x-ray spectra emitted from Maxwellian electrons always have positive values of κ as seen by the dotted curves in Fig. 9(a) as well as the fitting curves in Figs. 7(c) and 7(d). Such a spectrum with $\kappa < 0$ is one of the remarkable x-ray characteristics emitted from plateau-electron distributions as shown in Fig. 8. Therefore, we now use fitting curves from plateau electrons. The dashed curve shown in Fig. 9(b) is calculated using f_{ep} in Fig. 6(b); here, we use the data of $2\phi_{pb}=5.4$ kV for the potential-trapped plateau electrons along with the mirror-trapped Maxwellian with a 35° loss cone ($T_{pm}=60$ keV and 2.5% of the total plug density n_p). This fitting is based on the fact that dominant x-rays come from hot-core plasmas.

More detailed analyses for the x-ray spectra taking account of the radial profile of ϕ_{pb} are carried out using f_{ep} in Fig. 6(b). A line-integrated intensity at $h\nu$ with the x-ray PHA, $I_{XP}(h\nu)$, is written as

$$I_{XP}(h\nu) = \int (n_e n_i Z^2)(r) I_{XC}(h\nu, r) dr. \quad (1)$$

Here, $I_{xc}(h\nu, r)$ is calculated for $h\nu$ at a plasma radius r using the observed profile of ϕ_{pb} in Fig. 10(a) under our low-*Z* conditions; the intensities of $I_{xc}(h\nu, r)$ are normalized for unit values of electron and ion densities, n_e, n_i , and an ion effective charge *Z*. Tomographically reconstructed x-ray emissivity at r , $I_{XT}(r)$, is described as

$$I_{XT}(r) = (n_e n_i Z^2)(r) \int I_{XC}(h\nu, r) d(h\nu). \quad (2)$$

Here, $I_{XT}(r)$ is corrected by the absorber transmissivity and the MCP response [16–19].

Using Eqs. (1) and (2), we obtain

$$I_{XP}(h\nu) = \int \left[\left(I_{XT}(r) / \int I_{XC}(h\nu, r) d(h\nu) \right) \times I_{XC}(h\nu, r) \right] dr. \quad (3)$$

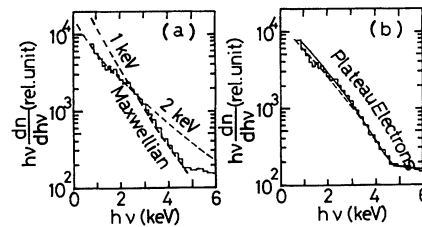


FIG. 9. (a) Data fitting using relativistic Maxwellian distributions with 2- and 1-keV temperatures. (b) The dashed curve is calculated using the strong ECH model shown in Fig. 6(b); here, data are fitted by plateau-electron distribution functions [the maximum energy of 5.4 keV ($=2\phi_{pb}$) on axis] along with the mirror-trapped Maxwellian electrons (2.5% to the total density, 60 keV with a loss-cone angle of 35°). In addition to the contribution of the on-axis electrons (the dashed curve), we take account of the contribution of the radial electron profile for the solid curve in (b); the ϕ_{pb} profile and the x-ray tomography data in Fig. 10 are used.

Therefore, the data from x-ray tomography for $I_{XT}(r)$ [Fig. 10(b)] and the data on $\phi_{pb}(r)$ [Fig. 10(a)] for calculating $I_{XC}(h\nu, r)$ predict the spectrum of $I_{XP}(h\nu)$ using Eq. (3); this calculated spectrum is shown by the solid curve in Fig. 9(b). Good agreement between the observed x-ray spectrum and the calculation in Fig. 9(b) indicates the validity of the strong ECH theory, which predicts the model in Fig. 6(b). Thus, it is again noteworthy that such x-ray observations of electron-velocity distribution functions as well as of electron spatial profiles are directly connected with a mechanism study of the potential formation [10] and a scaling study of ϕ_c vs ϕ_b , which is one of the most important scalings for tandem-mirror ion confinement.

From this viewpoint, it is useful to confirm this scaling theory using another independent method of comparing the x-ray data with the calculated x rays using the plateau-electron-velocity distributions. It is necessary to assume a low- Z (or a radially uniform Z) condition and a small contribution of high-energy electrons to the total x-rays (thereby $n_e = n_i$); these conditions are satisfied as described above. The x-ray emissivity profiles corrected by the effect of various thickness absorbers are calculated from

$$I_{XT}(r) = \int n_e(r) n_i(r) Z^2(r) I_{XC}(h\nu, r) d(h\nu). \quad (4)$$

The solid curves in Fig. 10(c) are the x-ray emissivity profiles calculated from Eq. (4) with various absorber characteristics. Here, we use the radial profile of ϕ_{pb} in Fig. 10(a) and the model in Fig. 6(b) as well as the profile of n_e deduced from x-ray data with a 1.8- μm PP absorber, which is sensitive to $n_e n_i Z^2$ but insensitive to $h\nu$ [7]. This shows the same profile as the density profiles measured with microwave interferometers in the barrier region and in the central cell. Good agreement between the profile data using the x-ray diagnostics and the calculations in Fig. 10(c) again proves the validity of the strong ECH plateau-formation theory.

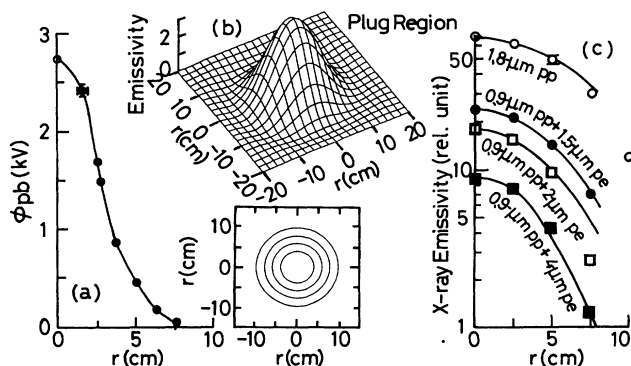


FIG. 10. (a) Radial profile data on ϕ_{pb} . (b) Tomographically reconstructed x-ray emissivity in the plug region using a 1.8- μm polypropylene absorber ($h\nu \gtrsim 80$ eV) along with a contour plot of the emissivity. (c) X-ray radial profile data with various absorbers are compared with the calculated x-ray profiles (solid curves) from the plateau-electron distribution functions using the ϕ_{pb} data in (a).

B. The electron-velocity distribution function in the barrier region and the effect of the electron spatial profile on plasma confinement

Figure 11(a) shows a typical x-ray spectrum from the NaI(Tl) detector. The dashed curves are calculated using relativistic Maxwellian electron distribution functions with temperatures T_{eh} of 50, 60, and 70 keV and a loss-cone angle θ_0 of 55°; this angle is estimated from the axial x-ray distribution in the barrier region [7,8]. In Fig. 11(b), individual x-ray components calculated for the spectrum fitting in Fig. 11(a) are shown; here we represent a typical case with $T_{eh} = 60$ keV and the ratio of n_{eh} to the total density n_b of 0.3 (see Ref. [7]). The solid curve in Fig. 11(b) shows total x-ray emissivity, which is composed of the x rays from interactions between the hot electrons and ions (the dashed curve labeled he-i), interactions between the hot electrons (the dashed curve labeled he-he), and interactions between the hot electrons and cold electrons (the dashed curve labeled he-ce). This value of T_{eh} in Fig. 11 is the same temperature of the high-energy electron component in the plug region (Fig. 7). From the fact that both electron components exist regardless of the formation and the disappearance of ϕ_b or ϕ_c , it is found that the high-energy electrons in each region are magnetically trapped in the plug and barrier mirror. Here, it is of importance to note the following relation between the barrier and the plug electrons: A fraction of the barrier hot electrons reaches the plug region and is represented in the domain M of Fig. 6(b). On the other hand, the plug electrons, which are produced and accelerated beyond the ellipsoidal boundary in Fig. 6(b) due to plug ECH, are confined in the plug and barrier mirror; then, these electrons with a

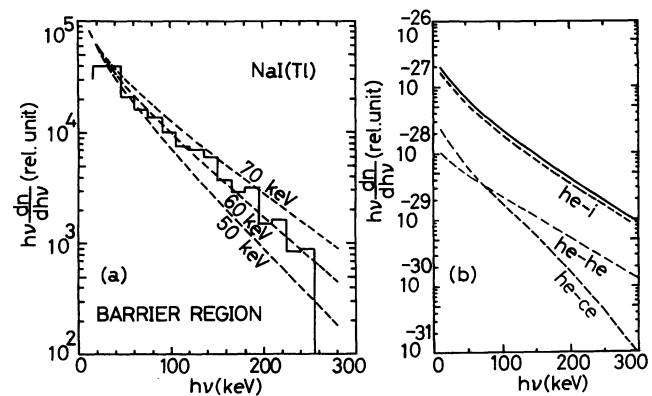


FIG. 11. (a) An x-ray energy spectrum in the barrier region using the NaI(Tl) detector. Data are fitted by relativistic Maxwellian electron distribution functions with T_{eh} of 50, 60, and 70 keV along with a loss-cone angle of 55°, as estimated by the x-ray axial profile. (b) Calculated x-ray components for the spectrum shown in (a) with $T_{eh} = 60$ keV, $n_{eh}/n_b = 0.3$, and $\theta_0 = 55^\circ$; total emissivity (solid curve), emissivity from interactions between the hot electrons and ions (the dashed curve labeled he-i), from interactions between the hot electrons (he-he), from interactions between the hot electrons and cold electrons (he-ce).

few keV of energy are strongly heated by both barrier and plug ECH along their bounce motions. These processes result in the formation of 60-keV electrons in the barrier region, and these electrons are shown in the region *M* of Fig. 6(b) as well. Thus, from the viewpoint of the production mechanism of the hot electrons, the barrier hot electrons in this section (III B) and the plug electrons described in Sec. III A are closely correlated with each other.

These magnetically trapped hot electrons then play an important role in the formation of ϕ_b [7]; therefore, the electrons accelerated by plug ECH may contribute not only to the formation of ϕ_c [see the region *P* in Fig. 6(b)] but also to the formation of ϕ_b [the region *M* in Fig. 6(b)].

Next, we briefly summarize the following characteristic features of the hot electrons from the barrier x-ray data for giving information on the overall characteristics of the barrier plasma parameters. The evolution of T_{eh} with time shows a saturation at $T_{eh} = 60$ keV, while their density n_{eh} successively increases with time; this fulfills the requirement of obtaining a large value of n_{eh} without increasing T_{eh} . The saturation of T_{eh} is desirable for MHD stability in the barrier region, since a magnetic-field line in the barrier region has a bad curvature. The increase in n_{eh} with time is convenient to obtain a high value of the ratio of n_{eh} to total density, since its large ratio makes a large value of ϕ_b [6].

The saturation mechanism of T_{eh} is explained using the conditions of second-harmonic ECH corrected for the effects of relativistic mass variation and Doppler shift (for more detailed discussion of these effects on the production of hot electrons, see Ref. [7]).

The spatial profile of the hot electrons and its effect on plasma confinement are studied using two-dimensional tomographic reconstructions of the x rays from the hot electrons (see Fig. 4) [20].

Figure 12(a) shows the magnetic-field lines (solid curves along the z axis) as well as the mod- B surfaces (solid curves across the z axis) in the barrier region. The location of $\omega \approx 2\Omega_e$ under standard operating conditions for the thermal-barrier formation ($B_m = 4.97$ kG) is pointed out along with the microwave lobe of barrier ECH (bounded region by the dashed lines). For reference, the location of $\omega \approx \Omega_e$ (the plug region) and the plug ECH lobe are also shown.

Under these conditions, the radial profiles of line-integrated x-ray data measured with the two sets of MCP's (Fig. 4) are plotted in Fig. 12(b); circles and triangles are the data from the diagnostic x-ray imaging systems XIS(A) and the XIS(B) in Fig. 4, respectively. These data are corrected using the calibration data of the MCP's [16–19]. Using these data, a tomographic reconstruction of the x-ray emissivity is generated in Fig. 12(c). Its contour map is also plotted in Fig. 12(d). This radial profile of the x-ray emissivity using a 1.5- μm -thick PE absorber (see Sec. II) is similar to those using a 5.5- μm PE absorber or a 50- μm Al absorber; this indicates a radially uniform electron temperature. This value is estimated to be 50–60 keV from these relative intensities (x-ray absorption method). This value of T_{eh} is con-

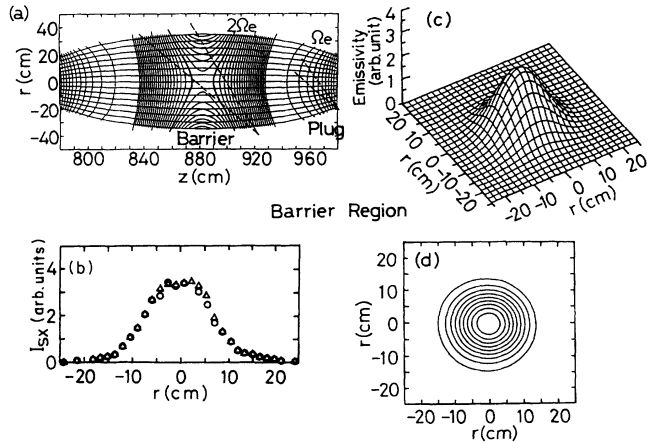


FIG. 12. (a) Magnetic-field lines (solid curves in the z direction) and mod- B surfaces (solid curves crossing the magnetic-field lines) in the plug and barrier mirror. Curves labeled $\omega = 2\Omega_e$ and Ω_e represent the locations of classical second-harmonic and fundamental electron cyclotron resonance layers, respectively, under the thermal-barrier operating conditions. Dashed lines show the incident microwave lobes of barrier and plug ECH. (b) Radial profile of line-integrated x rays in the midplane of the barrier region. The data are obtained by two x-ray imaging systems (see Fig. 4) using a 1.5- μm -thick polyester absorber. (c) A two-dimensional tomographically reconstructed x-ray emissivity plot. (d) Contour plot of x-ray emissivity.

sistently obtained from the radially scannable x-ray PHA system with the NaI(Tl) detector (Fig. 3) as well as the x-ray system with the pure Ge (Fig. 2) [7] [see again the spectrum ($r=0$) in Fig. 11].

It is also noted that the radial profile of the total density (being equivalent to n_i) measured with a microwave interferometer shows the same profile as the square root of the x-ray emissivity profile. Thus, the square root of the x-ray emissivity profile in Fig. 12(c) also shows the hot-electron density profile, since the x-ray emissivity is proportional to $n_i n_e$ under the condition of uniform T_{eh} as well as of uniform or small Z . These characteristics of Z in the barrier region are consistent with those in the plug region as described in Sec. III A.

Furthermore, these x-ray tomography data in Fig. 12 provide the following important information on the plasma potential and thereby on the tandem-mirror plasma confinement.

(i) The observed peaking profile of n_{eh} on the magnetic axis is desirable for the formation of ϕ_b in the core plasma region, since ϕ_b becomes larger with increasing n_{eh} . The scaling law in Fig. 5 shows that ϕ_c becomes larger with increasing ϕ_b [6]. Thus, this ϕ_b profile may result in the formation of large values of ϕ_c in the core plasma region as well. In fact, such a peaking profile of ϕ_c in the core region is observed with ELA [9]. (ii) Another characteristic feature in Fig. 12 is a good axisymmetric profile. It is reported that asymmetries of plasma densities, temperatures, or potentials may lead to the formation of local electric fields; they may cause nonambipolar radial particle losses [33]. From this viewpoint, the observed axisymmetric profile is desirable for preventing

such anomalous particle losses. In GAMMA 10, such radial particle losses have been observed to be small using particle-loss diagnostics [9]. (The effects of nonaxisymmetric components of potentials in some different tandem-mirror configurations are discussed in Ref. [33]).

C. The electron-velocity distribution function in the central cell

In this section the effects of the formation of ϕ_b and ϕ_{pb} (see Secs. III A and III B) on the central-cell and plug electrons are described in detail. We at first show a data set in Fig. 13. One of the characteristic features of the data is a fast rise of ϕ_b beyond 1 kV, and a subsequent gradual decrease in ϕ_b with time [Fig. 13(c)]. Figure 13 shows the following significant difference between electron energies in the central cell and in the plug region: An increase in the central-cell bulk electron temperature T_{ec} during the thermal-barrier period has been observed as measured with the x-ray diagnostics [Fig. 13(b)], while in contrast a temporal decrease in the plug electron energy has been observed [Fig. 13(d)]. As compared with the data in Figs. 13(d) and 13(e), the variation of the value of ϕ_{pb} is closely related to the plug electron energy. This fact also supports the validity of the strong ECH theory [10] from the following viewpoint: This theory predicts that the plug electrons trapped by ϕ_{pb} are confined within the ellipsoidal boundary in Fig. 6(b); the maximum energy of the ϕ_{pb} trapped electrons equals $2\phi_{pb}$ [10]. Thus, the sustenance of these plug electrons is strongly affected by the variation of the value of ϕ_{pb} , and thereby the plug electron energy immediately follows the temporal evolution of ϕ_{pb} . This feature can be seen in Figs. 13(d) and 13(e). Here, it is noted that the averaged energy of these plateau-shaped plug electrons may be defined as the ratio of the total electron energy to the total electron population, E/N . This value becomes $1.5 T_e$ for

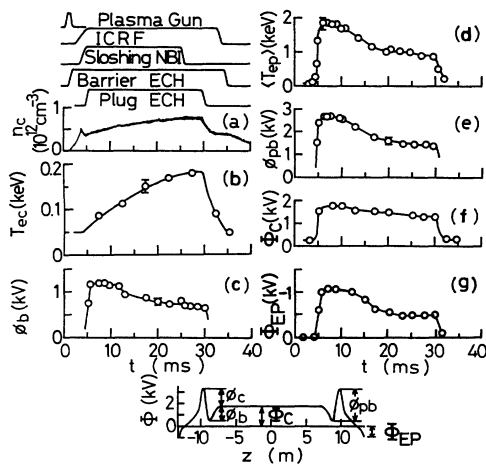


FIG. 13. Temporal evolution of (a) the central-cell density; (b) the central-cell bulk-electron temperature; (c) the thermal-barrier potential; (d) the effective plug temperature; (e) the plug electron-confining potential; (f) the central-cell warm-electron temperature; (g) its density; (h) the bulk-electron energy density; (i) the estimated values of τ_{Ee} from the power-balance equation in Eq. (5) (crosses), and from the Pastukhov theory in Eqs. (6) and (7) (circles). Discussions are also made in Sec. III D.

Maxwellian electrons, and E/N equals ϕ_{pb} for a plateau distribution. Therefore, we define the effective plug temperature $\langle T_{ep} \rangle$ by $\phi_{pb}/1.5$ so as to compare it with T_{ec} . An important feature of $\langle T_{ep} \rangle$ is again pointed out, namely that $\langle T_{ep} \rangle$ follows ϕ_{pb} immediately. This feature is consistently found from the fact that $\langle T_{ep} \rangle$ increases with time when ϕ_{pb} increases temporally (Fig. 14).

On the other hand, T_{ec} behaves in a quite different manner from $\langle T_{ep} \rangle$; T_{ec} increases both with decreasing ϕ_b (Fig. 13) and with increasing ϕ_b (Fig. 14), as long as the values of ϕ_b are maintained in the range of more than several hundred volts. Heating sources for the central-cell bulk electrons are estimated in the following. There are no direct electron-heating sources. However, the warm electrons from the plug region traveling through the plug loss cone [the region L in Fig. 6(b)] are an important heating source for the central-cell bulk electrons. These warm electrons in the central cell can heat the bulk electrons through a classical collisional energy-relaxation process [34]. Hot ions (~ 1 keV) in the central cell produced by ion-cyclotron heating is another heating source for the bulk electrons; however, the slowing down power of the hot ions is one to two orders of magnitude smaller than that of the warm electrons. For example, in the period $5 \text{ ms} < t < 15 \text{ ms}$, the slowing-down power of these ions contributes only a few percent to the total slowing down power. Also, the direct electron-heating power of electron Landau damping from slow ion-cyclotron waves is estimated to be a few orders of magnitude smaller than the slowing down power of the warm electrons because of the low values of the perpendicular refractive index and the electric-field intensity perpendicular to the magnetic field. Actually, this explains why there are no changes in the x-ray emissivity when ion-cyclotron heating power is varied during the thermal-

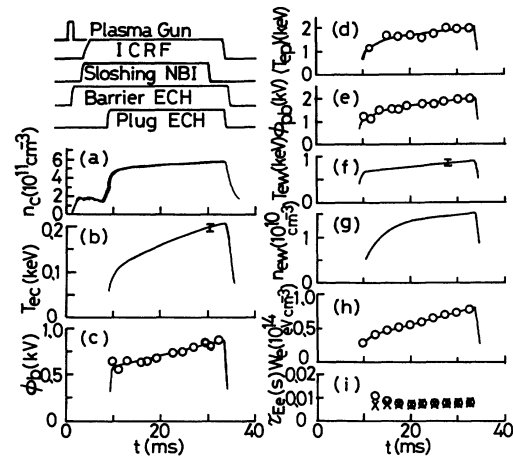


FIG. 14. Temporal evolution of (a) the central-cell density; (b) the central-cell bulk-electron temperature; (c) the thermal-barrier potential; (d) the effective plug temperature; (e) the plug electron-confining potential; (f) the central-cell warm-electron temperature; (g) its density; (h) the bulk-electron energy density; (i) the estimated values of τ_{Ee} from the power-balance equation in Eq. (5) (crosses), and from the Pastukhov theory in Eqs. (6) and (7) (circles). Discussions are also made in Sec. III D.

barrier period. Therefore, the precise observations of the parameters of the warm electrons as well as of the bulk electrons using several x-ray diagnostic techniques are essential to estimate the total heating power for the central-cell bulk electrons. Figure 13(g) stands for the absolute value of a floated-end-plate potential, ϕ_{EP} . (The effects of the end plates are described in Refs. [35–38].)

In Fig. 15 we plot the absorption characteristics for central-cell x rays measured with (a) the SSB detector [18,21] and (b) the MCP [16–19] as a function of the absorber thickness. Due to a good sensitivity to the kilo-electron-volt-range x rays as is obtained using synchrotron radiation [16–19,21], the SSB detector is employed particularly for the investigation of the warm electrons [13]. Furthermore, we show x-ray energy spectra in the central cell observed with the Si(Li) detector; these data are useful to analyze multi-component electron distribution functions. The SSB data in Fig. 15(a) (at $t = 17.5$ ms in Fig. 13) are fitted by 3-keV Maxwellian electrons using the four data points obtained with the thicker absorbers in order to avoid the effect of the bulk electrons on the data. By combining the SSB data measured with the thick and the thin absorbers, we can calculate the ratio of the population of the 3-keV electron component to the total density; here, the contribution of the x-ray emissivity from the 3-keV electrons to the data obtained with the thin absorbers is subtracted. These data indicate that the population of the 3-keV warm electrons is 2% of the central-cell total electron density. From the calibration data on the x-ray energy response of the MCP [16–19], the energy range of the x rays from the bulk electrons lies

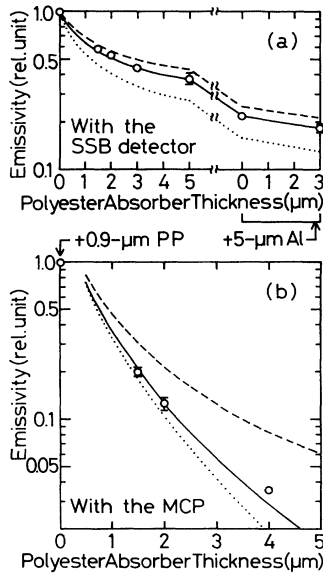


FIG. 15. X-ray energy analyses using the x-ray absorption method at 17.5 ms in Fig. 13. The solid curves in (a) and (b) show the x-ray emissivity calculated from the bulk electrons (150 eV, 98%) and the warm electrons (3 keV, 2%). In (a), the dashed and the dotted curves are calculated using 3% and 1% warm electrons, respectively. In (b), the dashed and the dotted curves are x-ray emissivity from 1-keV and 100-eV Maxwellian electrons, respectively.

in the sensitive energy region of the MCP, since the MCP has a higher gain even below a few hundred eV; this is a distinctive merit as compared with the other detectors. In Fig. 15(b) the solid curve shows the calculated x-ray emissivity from the bulk electrons (150 eV, 98%) and the warm electrons (3 keV, 2%). Thus, good agreement between the two data sets is obtained. Also, the data for electron-cyclotron emission agree well with the x-ray data [35]. This agreement, as well as the fact that there is no appreciable line radiation in the x-ray spectra of all cells (see Secs. III A and III B), means that the impurity concentration is quite small in the thermal-barrier operations (for more detail see Ref. [20]).

To obtain x-ray emissivity in Fig. 15, it is required to generate x-ray tomographic reconstructions. Figure 16(a) shows an example of a two-dimensional reconstruction of the emissivity obtained with a 0.9- μm PP absorber and a 1.5- μm PE absorber at $t = 15$ ms in Fig. 13. These tomography data are useful not only for analyzing electron temperatures on axis (Fig. 15) but also for giving information on spatial distributions of electrons.

These x-ray tomographic reconstructions represented in Figs. 10(b), 12(c), and 16(a) provide a spatial data set for the electrons in the main regions of a tandem mirror (namely, from the central-cell through the thermal-barrier region to the plug region).

Using the tomography data observed with various absorbers, we obtain radial profiles of T_{ec} as shown in Fig. 16(b). It is noted that the solid and dashed curves represent the data with and without the formation of ϕ_b , respectively. The radial positions where the increase in T_{ec} is observed with the formation of ϕ_b [Fig. 16(b)] correspond to the locations with the formation of ϕ_{pb} [Fig. 10(a)]. This correlation is consistently understood when we remember the relation of $\phi_{pb} = \phi_c + \phi_b$ and the scaling of ϕ_c vs ϕ_b .

The data represented in Figs. 13 and 15 are also cross-checked using x-ray energy spectra observed with the Si(Li) detector (Fig. 17). An example of the spectra in Fig. 17 corresponds to the data at $t = 20.5$ – 22.5 ms in Fig. 13. Here, we use the same method which is em-

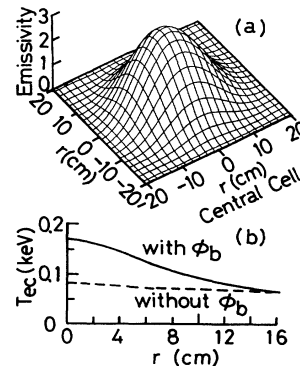


FIG. 16. (a) Tomographically reconstructed x-ray emissivity in the central cell using a 0.9- μm PP absorber and a 1.5- μm PE absorber at $t = 15$ ms in Fig. 13. (b) Radial profiles of the central-cell bulk-electron temperature with (solid curve) and without (dashed curve) thermal-barrier potentials.

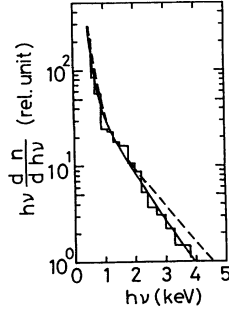


FIG. 17. An x-ray energy spectrum in the central cell using the Si(Li) detector. For the solid curve, radial profiles of plasma parameters are taken into account (see Figs. 13, 16, and 18). For reference, the dashed curve is calculated using the on-axis parameters alone.

ployed for analyzing the data in Fig. 9. The solid curve is calculated using the parameters represented in Fig. 13 and their radial profiles from the x-ray tomography as well as further information on the warm-electron temperature T_{ew} [Figs. 18(a) and 18(c)] and on the warm-electron density n_{ew} [Figs. 18(b) and 18(d)]. These values of T_{ew} and n_{ew} are consistently obtained using the above described three types of x-ray detectors. Here, for reference, the spectrum calculated from the on-axis parameters alone is also shown by the dashed curve in Fig. 17; that is, the radial profile data are not taken into account for the dashed curve. In Fig. 17 the x-ray spectrum is well fitted by the solid curve; whereas, the dashed curve

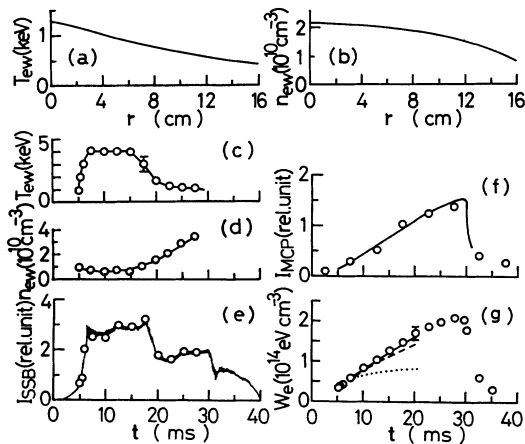


FIG. 18. Radial profiles of (a) the warm-electron temperature T_{ew} and (b) its density n_{ew} in the central cell ($t=20.5-22.5$ ms in Fig. 13) along with the temporal evolution of (c) T_{ew} and (d) n_{ew} . (e) X-ray data with the SSB detector using a combination of a $0.9\text{-}\mu\text{m}$ PP, a $3\text{-}\mu\text{m}$ PE, and a $5\text{-}\mu\text{m}$ Al absorber are fitted by the intensities (circles) calculated from the analyzed parameters in Figs. 13 and 18. (f) The tomographically reconstructed x-ray data on axis using the MCP with a $0.9\text{-}\mu\text{m}$ PP and a $1.5\text{-}\mu\text{m}$ PE absorber (circles) are fitted by the x-ray emissivity (solid curve) calculated from the data in Figs. 13 and 18. (g) The bulk-electron energy density from the data in Figs. 13(a) and 13(b). The solid, dashed, and dotted curves correspond to the values of $\tau_{Ee} = 0.1, 0.04,$ and 0.01 s, respectively.

overestimates the data particularly on the high-energy component ($h\nu \gtrsim 2$ keV). This is reasonable since the actual values of T_{ew} decrease radially. However, the information on the radial profiles is not included for the dashed curve. This indicates the usefulness and the necessity of the x-ray tomography data when we strictly analyze the x-ray energy spectrum data.

To check again these analyzed plasma parameters from Figs. 13 to 18(d), the SSB data in Fig. 18(e) obtained with thick absorbers (a combination of a $0.9\text{-}\mu\text{m}$ PP, a $3\text{-}\mu\text{m}$ PE, and a $5\text{-}\mu\text{m}$ Al absorber) are utilized; this cross-check is made particularly for the confirmation of the analyzed results of the warm-electron component. The SSB data in Fig. 18(e) agrees well with the x-ray intensities (circles) calculated from the analyzed parameters in Figs. 13(a), and 18(a)–18(d). The evolution of the tomographically reconstructed data using the MCP with a $0.9\text{-}\mu\text{m}$ PP and a $1.5\text{-}\mu\text{m}$ PE absorber (circles) in Fig. 18(f) also agrees well with the x-ray emissivity (solid curve) calculated from the data analyzed in Figs. 13(a), 13(b), and 18(a)–18(d).

Here, it is important to note that x-ray PHA data represented in Figs. 7, 11, and 17 provide information on various types of electron-velocity distribution functions in each cell of a tandem mirror. It is worth noting that each region has its differently characterized distribution function; that is, the two-component Maxwellian electrons in the central cell, the relativistic Maxwellian electrons in the barrier region, as well as the electrons in the shape of a plateau-electron distribution function in the plug region. These electrons are directly connected through magnetic-field lines; however, they are separated by the kilovolt-range electrostatic potentials. In particular, the thermal-isolation effect due to the formation of thermal-barrier potentials has been clearly demonstrated by the observations not only of a significant difference between the electron energies in the central cell and in the plug region but also of the different shapes of the electron distribution functions in these two regions which are separated by the thermal barrier.

D. Electron-energy confinement due to the formation of thermal-barrier potentials

In Secs. III A–III C the detailed data on electrons in the three different regions are described individually. The mutual relations between each electron distribution function are discussed in this section. The energy balance for the bulk electrons confined by ϕ_b is also investigated. These electrons with three different shapes of distribution functions are closely related with one another, and these relations are summarized as follows: The relativistic hot electrons in the barrier region play an important role in the formation of ϕ_b , and then the plateau electrons in the plug region are formed with the associated enhancement of ϕ_c due to ϕ_b (a thermal-isolation effect). A fraction of the plug electrons flowing into the central cell forms a warm-electron component in the central-cell electrons; this component becomes a heating source for the central-cell bulk electrons (see Secs. III A and III C).

The formulation of the power balance is as follows: In general, the energy-balance equation for the bulk-electron energy density W_e is written as

$$\frac{dW_e V_{bb}}{dt} = P_{wb} V_{bb} + P_{hb} V_{cc} - \frac{W_e V_{bb}}{\tau_{Ee}}, \quad (5)$$

where P_{wb} and P_{hb} are the input powers to the bulk electrons through energy-relaxation processes from the warm-electron component originated from the plug region [Figs. 18(c) and 18(d)] and from the hot ions produced by ion-cyclotron heating in the central cell, respectively. The volumes of the ϕ_b confined electrons and the central-cell hot ions are denoted by V_{bb} and V_{cc} , respectively. The values of W_e [Fig. 18(g)] are obtained from the parameters in Figs. 13(a) and 13(b). The remaining parameter in Eq. (5) is only the total electron-energy confinement time τ_{Ee} ; it is noted that all electron-energy losses through whatever process are represented by this overall confinement time τ_{Ee} . For example, one of the loss processes is radiation energy loss, which is estimated to be several orders of magnitude smaller than the input energy of P_{wb} . However, according to the definition of Eq. (5), such loss processes are automatically included in the third term on the right-hand side of Eq. (5).

For the terms of input powers in Eq. (5), P_{wb} is one to two orders of magnitude larger than P_{hb} . (Relaxation powers from sloshing ions to the bulk electrons are much smaller than P_{hb} , since the sloshing ions have higher energy and lower density as compared with the central-cell hot ions.) In addition, V_{bb} is larger than V_{cc} . As mentioned earlier, the power of electron Landau damping from ion-cyclotron waves is negligible and other direct electron-heating processes are not expected.

Thus, under our experimental conditions, dominant parameters in Eq. (5) are W_e , P_{wb} , and τ_{Ee} alone. Using the temporal variations of the data in Figs. 13 and 15–18, the fitting curves to W_e then depend only on the values of τ_{Ee} . The solid, dashed, and dotted curves in Fig. 18(g) correspond to the values of $\tau_{Ee} = 0.1, 0.04,$ and 0.01 s, respectively. The fitting of the data shows good electron-energy confinement ($\tau_{Ee} > 0.1$ s), which is due to the thermal-barrier potentials in the kilovolt range. On the other hand, τ_{Ee} is calculated to be more than 0.1 s from the Pastukhov theory [14] modified by Cohen *et al.* [15]. Therefore, the data represented here show a good confinement property for the ϕ_b confined electrons, as predicted by the Pastukhov theory.

A similar time scale for ion-energy confinement has been obtained in a recent study [38] in which a very-low-level density fluctuation during the thermal-barrier period has been observed. This suggests that there exist no large magnetohydrodynamic (MHD) instabilities during the thermal-barrier operations. Hence, it can also be expected that there is no anomalous electron-energy transport driven by such instabilities in the thermal-barrier operations.

A data set in Fig. 14 has two important characteristic features. First, the comparison of different temporal evolutions of ϕ_b as well as ϕ_{pb} in Figs. 13 and 14 provides important information on the roles of the potentials in

electron-energy confinement. In contrast to the temporal decrease of ϕ_{pb} and ϕ_b in Fig. 13, both of ϕ_{pb} and ϕ_b in Fig. 14 increase with time. In these data, a remarkably different behavior of $\langle T_{ep} \rangle$ from that of T_{ec} is found. These differences confirm the discussion in Fig. 13; that is, $\langle T_{ep} \rangle$ immediately follows the variation of ϕ_{pb} with time, while, T_{ec} increases in either case with increasing or decreasing ϕ_b as far as the condition of $\phi_b/T_{ec} \gg 1$ is maintained. This strong correlation between the values of $\langle T_{ep} \rangle$ and ϕ_{pb} is explained by the strong electron acceleration due to plug ECH up to the ellipsoidal boundary with the maximum energy of $2\phi_{pb}$ [see again Fig. 6(b)]. On the other hand, a strong thermal-isolation effect due to the formation of ϕ_b may result in the different behavior of T_{ec} from that of $\langle T_{ep} \rangle$. The volume of the central-cell bulk electrons are much larger than the volume of the plug electrons, and the heating source for these ϕ_b -confined bulk electrons is much smaller than the plug electron heating power. Therefore, as long as the value of ϕ_b/T_{ec} is sufficiently larger than unity, an increase or a decrease in ϕ_b with time does not strongly affect the behavior of T_{ec} . This feature is understood in the following. In the case of $\phi_b/T_{ec} \approx 1$, T_{ec} strongly depends on ϕ_b , since the electron-confinement ‘‘capability’’ determined by ϕ_b becomes comparable to the confined-electron ‘‘activities’’ represented by T_{ec} . In this case, heating powers are lost with the electrons beyond the low potential barriers, since the height of ϕ_b is comparable to the electron energies; therefore, T_{ec} does not increase yet. Thus, this means that the continuous increase in T_{ec} with time may be expected as far as the potentials of ϕ_b work as electron confining barriers with large values of ϕ_b/T_{ec} .

Therefore, from the above data comparisons between $\langle T_{ep} \rangle$ and T_{ec} using the different time evolution of ϕ_b or ϕ_{pb} in Figs. 13 and 14, we again confirm the essential role of ϕ_b in the thermal-isolation effect.

Another characteristic feature of the data in Fig. 14 comes from temporal increases in both parameters of ϕ_b and T_{ec} . According to the following Pastukhov formula for τ_{Ee} , nearly a constant value of τ_{Ee} with time during the thermal-barrier period is obtained although the absolute values of ϕ_b (thereby τ_{Ee}) are smaller as compared with those in Fig. 13.

The Pastukhov theory [14] modified by Cohen *et al.* [15] gives the following formula for the electron-particle confinement time τ_{pe} :

$$\tau_{pe} = \frac{\sqrt{\pi}}{4} \tau_{ee} \left[\frac{\phi_b}{T_{ec}} \right] \exp \left[\frac{\phi_b}{T_{ec}} \right] \frac{G(R)}{I(T_{ec}/\phi_b)}, \quad (6)$$

where

$$G(R) = \sqrt{1+1/R} \ln[(\sqrt{1+1/R} + 1)/(\sqrt{1+1/R} - 1)],$$

and

$$I(x) \approx \left[1 + \frac{x}{2} \right] / \left[1 + \frac{x^2}{4} \right].$$

Here, τ_{ee} is the collision time between the bulk electrons and R denotes the mirror ratio. The theoretical relation

between τ_{Ee} and τ_{pe} is described as

$$\tau_{Ee} = \tau_{pe} / \left[1 + \frac{2}{3} \left(\frac{\phi_b}{T_{ec}} \right) / I \left(\frac{T_{ec}}{\phi_b} \right) \right] \approx \frac{3}{2} \frac{\tau_{pe}}{1 + \phi_b/T_{ec}}. \quad (7)$$

From Eq. (7), a constant value of τ_{Ee} with time is expected from the data in Fig. 14; this is examined using the electron power balance [Eq. (5)]. The time scale of the first term on the right-hand side in Eq. (5) is the temperature relaxation time between the warm electrons and the bulk electrons; this is about one-half of a ms. The contribution of the second term is less than one order of magnitude as compared with that of the first term. Therefore, to obtain the values of the time derivative of W_e on the left-hand side in Eq. (5), the time duration for the fitting of dW_e/dt [Fig. 14(h)] is required to be a few times longer than one-half of a ms; that is, the characteristic time of the main energy input process in Eq. (5) is sufficiently shorter than the data-fitting duration for obtaining the values of dW_e/dt . Furthermore, Fig. 14(h) has a convenient feature for analyzing τ_{Ee} , since the data on W_e in Fig. 14(h) have a slow time variation compared with the duration for the data fitting (namely, a constant value of τ_{Ee} during the data fitting). The solid curve in Fig. 14(h) corresponds to a τ_{Ee} value of 8 ms; this constant value of τ_{Ee} with time is consistent with the estimated value from the Pastukhov theory. In Fig. 14(i), the estimated values of τ_{Ee} from the power balance using Eq. (5) (crosses) and from the Pastukhov theory in Eqs. (6) and (7) (circles) are compared; good agreement between the two has been confirmed for the first time.

In Fig. 19, using several similar data sets, we compare the values of τ_{Ee} obtained from the power balance analyses, τ_{Ee}^{PB} , with those calculated from the Pastukhov theory, τ_{Ee}^{Pastu} , in the range of more than three orders of magnitude. Good agreement between the two has shown the first evidence of the existence of a scaling law between

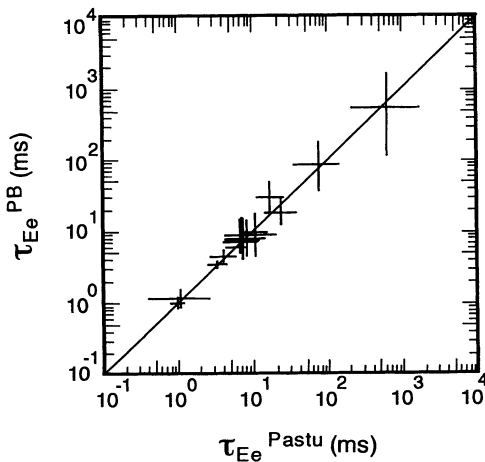


FIG. 19. The values of τ_{Ee} obtained from the power-balance analyses, τ_{Ee}^{PB} , are compared with those calculated from the Pastukhov theory, τ_{Ee}^{Pastu} .

τ_{Ee} and ϕ_b in a tandem mirror. Furthermore, the Pastukhov theory is constructed under the condition of a negligible radial loss, while the values of τ_{Ee} from the power-balance equation of Eq. (5) are determined by overall loss processes, including a radial loss. Therefore, Fig. 19 also suggests that the dominant loss process is still an axial energy loss in this range of τ_{Ee} [38,39].

Summarizing the data in Secs. IIIA–IIIC obtained with a combination of several types of x-ray diagnostics, we can make a qualitative picture for the confinement of potential trapped electrons due to thermal barriers: The electrons produced in the central cell are confined by thermal barriers, which are formed by barrier-mirror trapped hot electrons due to barrier ECH. A fraction of warm electrons produced by strong plug ECH falls into plug loss cone and flows into the central cell; these warm electrons in turn heat the ϕ_b -confined bulk electrons through the Coulomb energy-relaxation process. The energy-confinement time for the ϕ_b -confined bulk electrons is explained by the Pastukhov theory.

Here, it is noted that when these electrons are lost beyond the thermal barriers after their confinement time, they become sources for plug electrons or barrier electrons since intense microwaves for ECH in each region await these electrons from the central cell. Thereby, these loss electrons are immediately heated, and then some of them are trapped in the plug and barrier mirror or in the plug region (see Sec. IIIA); in these cases, the loss electrons change their energies due to ECH. In fact, we have never measured the plug electron component with the same temperature of the central-cell bulk electrons (see Sec. IIIA). This is an important and a convenient feature of the loss electrons from the central cell; that is, even if these electrons return to the central cell due to any unknown electron confining mechanisms existing outside of the plug region, these loss electrons are never counted as the central-cell bulk electrons because of their different temperature from T_{ec} . In other words, plug ECH works like a “sink” for the central-cell bulk electrons lost beyond ϕ_b . This role of ECH provides clear experimental data on the energy confinement due to ϕ_b for the central-cell bulk electrons.

The final brief note is made for MHD stability of the data shown in Figs. 13 or 14. In these low-density operations with a total β value of less than 0.5% along the central cell and the barrier regions (see Fig. 1), no interchange instability [4] is observed although anchor neutral-beam injection (NBI), as well as anchor ECH prepared for future high- β operations as MHD stabilizer, is not applied. At this time, theoretical researches into anchor stabilization are being developed in GAMMA 10. A recent preliminary report suggests the importance of the finite-Larmor-radius effect for stabilizing such low- β plasmas [40]. However, it is quite important to do further detailed research, including a line-tying stabilization effect [41] through halo plasmas and the axial flow of ECH produced warm electrons bouncing between both ends [see Fig. 13(g)], since metal end plates in both ends and metal limiters in each region exist. Also, a ponderomotive stabilization effect due to the incident ion-cyclotron waves in the central cell [42,43] provides

another possibility for MHD stabilization. For understanding such a stability issue quantitatively, future detailed measurements of halo-plasma parameters and ion-cyclotron range of frequencies (ICRF) wave-field intensities are necessary. A systematic investigation in MHD stability will become one of the most important issues, particularly for attaining high- β stable tandem-mirror operations in the future.

IV. SUMMARY

X-ray diagnostics, combined with the observations of x-ray energy spectra and x-ray tomographic reconstructions in the central cell, the thermal-barrier region, and the plug region, have clarified the following effects of kilovolt-range electrostatic potentials on electron-velocity distribution functions and on electron-energy confinement. Also, the relations between the parameters in each region and the scaling laws for the potentials and the energy confinement have been investigated using the x-ray data.

(1) A presentation of the data set on the electron-velocity distribution functions in all of the main regions of a tandem mirror has been made; each distribution is found to be different not only in their energies but also in their shapes, although these regions are directly connected through magnetic field lines. (i) In the barrier region, mirror-trapped hot electrons with 60-keV energies (a relativistic Maxwellian distribution with a loss cone) are produced for the formation of a thermal-barrier potential. (ii) In the plug region, a plateau-shaped electron-velocity distribution function produced by strong-plug ECH has been observed for the first time. These electrons are confined within the ellipsoidal boundary in the plug electron-velocity space; the boundary is determined by ϕ_{pb} [Fig. 6(b)]. For a fraction of the electrons heated beyond the boundary, they are trapped by the plug and barrier magnetic mirror; this component bouncing through the barrier region is heated up and becomes the mirror-trapped hot electrons with 60-keV energy due to the barrier ECH [the region *M* in Fig. 6(b)]. A fraction of the electrons is lost through the plug loss cone [the region *L* in Fig. 6(b)] and flows into the central cell. (iii) In the central cell, these kilo-electron-volt-range warm electrons from the plug region and the bulk electrons with a few hundred eV have formed two-component Maxwellian electrons. The warm electrons in turn become a dominant heating source for the bulk electrons through classical Coulomb energy-relaxation processes.

(2) The following different behavior of T_{ec} and $\langle T_{ep} \rangle$ with time has been observed: The temporal evolution of $\langle T_{ep} \rangle$ is closely related to the temporal variation of ϕ_{pb} . However, T_{ec} increases with time regardless of an increase or a decrease in ϕ_b as long as the values of ϕ_b/T_{ec} are maintained to be sufficiently larger than unity.

The different behavior of T_{ec} and $\langle T_{ep} \rangle$ as well as their

different shapes and energies of the velocity distribution functions has demonstrated the existence of the thermal-isolation effect due to ϕ_b between the central cell and the plug region.

(3) The presentation of x-ray tomography data all through the main regions of a tandem mirror [i.e., the thermal-barrier region (Fig. 12), the plug region (Fig. 10), and the central cell (Fig. 16)] have shown good axisymmetric profiles of electrons in each region; these axisymmetries prevent the formation of local nonaxisymmetric electric fields, which may degrade particle confinement through the nonambipolar radial-loss process [33].

(4) These tomographically reconstructed profiles have also shown the following features. (i) Hot electrons in the barrier region are peaked on the magnetic axis (Fig. 12); this profile is desirable for thermal-barrier formation in the core plasma, and thereby for the formation of ϕ_c or ϕ_{pb} in the core region of the plug plasmas through the scaling relation between ϕ_c and ϕ_b (Fig. 5). (ii) The radial profile of the plug electrons is actually observed to be peaked on the magnetic axis (Fig. 10). The radial profile of their energies is consistently explained by the ϕ_{pb} profile (Fig. 10) using Cohen's strong ECH model [Fig. 6(b)]. (iii) Tomography data in the central cell have shown that the region having an increase in T_e during the thermal-barrier period corresponds to the regime with the formation of ϕ_b (Fig. 16).

(5) Using these x-ray data, the following scaling laws have been obtained. (i) The theoretically predicted values of the energy-confinement time τ_{Ee} for the ϕ_b -confined bulk electrons [the Pastukhov theory modified by Cohen *et al.* in Eqs. (6) and (7)] have been found for the first time to be in good agreement, in the range of more than three orders of magnitude, with the values of τ_{Ee} estimated from the energy-balance equation in Eq. (5) (Fig. 19). The validity of the Pastukhov theory for τ_{Ee} also shows the existence of a scaling relation between τ_{Ee} and ϕ_b/T_{ec} . These data indicate a good electron-confinement property due to ϕ_b . (ii) The x-ray observation of a plateau-shaped plug electron-velocity distribution function for the ϕ_{pb} trapped electrons along with the relation between ϕ_c and ϕ_b (Fig. 5) consistently supports the validity of Cohen's strong ECH theory for the ion-confining-potential enhancement.

ACKNOWLEDGMENTS

The authors would like to acknowledge the members of the GAMMA 10 Group for their collaboration, particularly Professor T. Tamano, Dr. M. Ichimura, Dr. A. Itakura, Dr. I. Katanuma, Dr. Y. Nakashima, Ms. H. Hirata, and Dr. T. Kato of the National Institute for Fusion Science (NIFS), as well as Professor S. Tanaka of Kyoto University.

*Permanent address: Graduate School of Science and Technology, Niigata University, Niigata, Japan.

†Permanent address: National Institute for Fusion Science, Nagoya, Japan.

‡Permanent address: Japan Atomic Energy Research Institute, Naka Fusion Research Establishment, Ibaraki, Japan.

[1] R. M. Gilgenbach *et al.*, Phys. Rev. Lett. **44**, 647 (1980).

- [2] A. C. England *et al.*, Nucl. Fusion **29**, 152 (1989).
- [3] T. Cho and S. Tanaka, Phys. Rev. Lett. **45**, 1403 (1980).
- [4] T. Cho *et al.*, Nucl. Fusion **26**, 349 (1986).
- [5] K. Ogura, H. Tanaka, S. Ide, M. Iida, K. Hanada, M. Yoshida, T. Minami, T. Cho, M. Nakamura, T. Maekawa, Y. Terumichi, and S. Tanaka, Nucl. Fusion **31**, 1015 (1991).
- [6] For a recent detailed review of tandem mirrors, the readers can be referred to R. F. Post, Nucl. Fusion **27**, 1579 (1987).
- [7] T. Cho *et al.*, Nucl. Fusion **27**, 1421 (1987).
- [8] M. Hirata *et al.*, Jpn. J. Appl. Phys. **28**, 96 (1989).
- [9] T. Cho *et al.*, Nucl. Fusion **28**, 2187 (1988).
- [10] R. H. Cohen, Phys. Fluids **26**, 2774 (1983).
- [11] J. Lohr *et al.*, Phys. Rev. Lett. **60**, 2630 (1988).
- [12] T. Cho *et al.*, Phys. Rev. Lett. **64**, 1373 (1990).
- [13] M. Hirata *et al.*, Nucl. Fusion **31**, 752 (1991).
- [14] V. P. Pastukhov, Nucl. Fusion **14**, 3 (1974).
- [15] R. H. Cohen, M. E. Rensink, T. A. Cutler, and A. A. Mirin, Nucl. Fusion **18**, 1229 (1978); R. H. Cohen, *ibid.* **19**, 1295 (1979); **19**, 1693 (1979).
- [16] M. Hirata *et al.*, Rev. Sci. Instrum. **61**, 2566 (1990).
- [17] N. Yamaguchi *et al.*, Rev. Sci. Instrum. **60**, 368 (1989); **60**, 2307 (1989).
- [18] T. Cho *et al.*, Rev. Sci. Instrum. **59**, 2453 (1988); **60**, 2337 (1989).
- [19] T. Kondoh *et al.*, Rev. Sci. Instrum. **59**, 252 (1988).
- [20] T. Kondoh *et al.*, J. Appl. Phys. **67**, 1694 (1990).
- [21] T. Cho *et al.*, Nucl. Instrum. Methods **A289**, 317 (1990).
- [22] J. H. Foote, T. Cho, Y. Nakashima, K. Ishii, and S. Miyoshi, Bull. Am. Phys. Soc. **32**, 1884 (1987).
- [23] K. Ishii *et al.*, Rev. Sci. Instrum. **60**, 3270 (1989).
- [24] R. H. Cohen *et al.*, Nucl. Fusion **20**, 1421 (1980); **23**, 1301 (1983).
- [25] R. H. Cohen, and L. L. LoDestro, in *Physics of Mirrors, Reversed Field Pinches and Compact Tori*, Proceedings of the International School of Plasma Physics, edited by S. Ortolani and E. Sindoni (Società Italiana di Fisica, Bologna, 1987), Vol. II, p. 1187.
- [26] H. Bethe and W. Heitler, Proc. R. Soc. London, Ser. A **146**, 83 (1934).
- [27] R. L. Gluckstern, M. H. Hull, Jr., and G. Breit, Phys. Rev. **90**, 1026 (1953); **90**, 1030 (1953).
- [28] A. C. England and G. R. Haste, Phys. Rev. A **7**, 383 (1973); **8**, 1475 (1973).
- [29] G. Elwert, Ann. Phys. (Leipzig) **34**, 178 (1939).
- [30] K. Masai, S. Hayakawa, H. Itoh, and K. Nomoto, Nature (London) **330**, 235 (1987); **335**, 804 (1988).
- [31] K. Masai, Astrophys. Space Sci. **98**, 367 (1984).
- [32] T. Kato *et al.*, Phys. Rev. A **36**, 795 (1987).
- [33] I. Katanuma *et al.*, Phys. Fluids B **1**, 1459 (1989).
- [34] D. V. Sivukhin, in *Reviews of Plasma Physics*, edited by M. A. Leontovich (Consultants Bureau, New York, 1966), Vol. 4, p. 93.
- [35] T. Cho *et al.*, in *Proceedings of the Eleventh International Conference on Plasma Physics and Controlled Nuclear Fusion Research, Kyoto, 1986*, edited by J. W. Weil and M. Demir (IAEA, Vienna, 1987), Vol. 2, p. 243.
- [36] T. Kariya *et al.*, Phys. Fluids **31**, 1815 (1988).
- [37] Y. Kiwamoto *et al.*, J. Phys. Soc. Jpn. **58**, 2619 (1989).
- [38] A. Mase *et al.*, Phys. Rev. Lett. **64**, 2281 (1990).
- [39] S. Miyoshi *et al.*, in *Proceedings of the Thirteenth International Conference on Plasma Physics and Controlled Nuclear Fusion Research, Washington, DC, 1990*, edited by J. Weil and M. Spak, (IAEA, Vienna, 1991), Vol. 2, p. 539.
- [40] H. Hojo *et al.*, NIFS Report No. NIFS-98, 1991 (unpublished).
- [41] H. L. Berk *et al.*, Phys. Fluids **27**, 2705 (1984).
- [42] R. A. Breun *et al.*, in *Proceedings of the Eleventh International Conference on Plasma Physics and Controlled Nuclear Fusion Research, Kyoto, 1986*, edited by J. W. Weil and M. Demir (IAEA, Vienna, 1987), Vol. 2, p. 263.
- [43] Y. Yasaka and R. Itatani, Nucl. Fusion **24**, 445 (1984); **25**, 29 (1985); Phys. Rev. Lett. **56**, 2811 (1986).

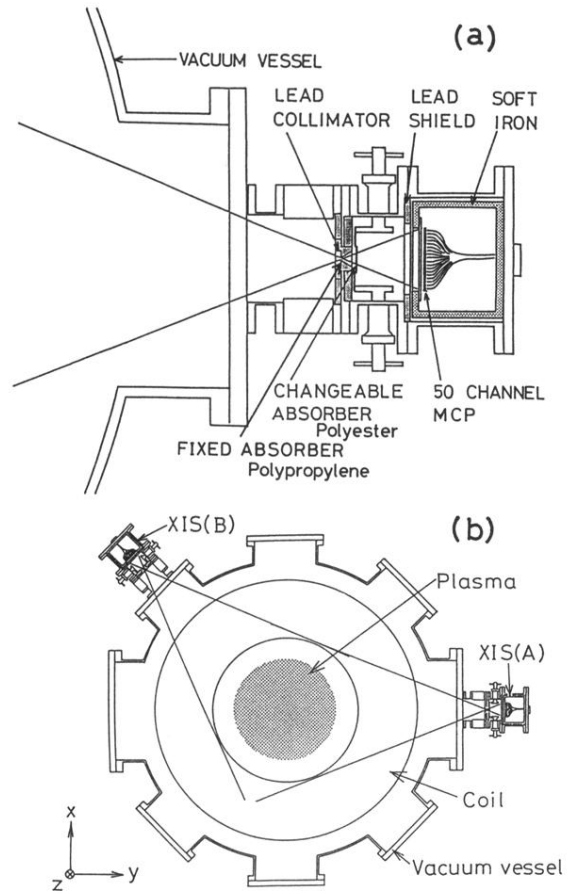


FIG. 4. Schematic view of (a) temporally and spatially resolved x-ray imaging system (XIS) with a multiple-anode microchannel plate (MCP), and (b) two sets of x-ray tomography systems (50 channels for each system).